PCCP

PAPER

View Article Online
View Journal | View Issue

Cite this: *Phys. Chem. Chem. Phys.*, 2023, **25**, 22523

Mechanism of formation of Co–Ru nanoalloys: the key role of Ru in the reduction pathway of Co†

Brandon Azeredo,[ab] Tayssir Ben Ghzaiel,[a] Ning Huang,[a] Sophie Nowak,[a] Jennifer Peron,[a] Marion Giraud,[a] Jeyadevan Balachandran,[c] Olivier Taché,[d] Laurent Barthe,[e] Jean-Yves Piquemal,*[a] Valérie Briois[e] and Lorette Sicard *[a]

Received 31st May 2023,
Accepted 7th August 2023

DOI: 10.1039/d3cp02522e

rsc.li/pccp

The chemical synthesis of alloy nanoparticles requires adequate conditions to enable co-reduction instead of separate reduction of the two metal cations. The mechanism of formation of bimetallic cobalt–ruthenium nanoalloys by reducing metal salts in an alcohol medium was explored to draw general rules to extrapolate to other systems. The relative kinetics of the reduction of both metal cations were studied by UV-visible and *in situ* Quick-X-ray absorption spectroscopies as well as H_2 evolution. The addition of Co(II) ions does not influence the reduction kinetics of Ru(III) but adding Ru(III) to a Co(II) solution promotes the reduction of cobalt cations. Indeed, while CoO is formed when reaching the boiling temperature of the solvent for the monometallic system, a direct reduction of Co is observed at this temperature without formation of the oxide for the bimetallic one. The co-reduction of the metal cations results in the formation of bimetallic nanoplatelets, the size of which can be tuned by changing the Ru content.

1. Introduction

Metal nanocrystals (NC) display intriguing properties, which are often different from their bulk counterparts, due to the high specific surface area and quantum size effects. The immense progress that has been made over the past 20 years in synthesizing them using liquid phase processes with precise control over the size and shape opens a broad range of applications in magnetism, optics, electronics, and catalysis.[1–9] The development of bimetallic NC is a step forward: they often do not display only a combination of the monometallic properties but also synergetic or new ones[10–13] which are particularly valuable in catalysis.[13–15] However, their synthesis is also trickier. It is generally performed by co-reduction of the two metal salts, thermal decomposition of organometallic precursors, seeded growth or a galvanic replacement reaction.[10] The polyol method has been revealed to be interesting among the co-reduction processes. This method refers to the reduction of metal salts in a poly-alcohol that acts as the solvent, the reductant as well as a complexing agent.[16] In this synthesis method, which can be extended to the reduction in monoalcohol media, the relative reduction kinetics of the two metal salts can be varied by changing the nature of the counterions and the solvent used, as well as the addition of ligands.[17–21] Even two non-miscible metals, for example Cu and Ag[22] or Ru and Cu,[23] could form nanoalloys.

Ru[24] and Co[25] nanoparticles (NPs) are widely used in catalysis and, by combining them into nanoalloys, we can expect strong improvement of their catalytic properties. For instance a small amount of Ru is added to Co-based Fischer Tropsch catalysts to enhance their stability.[26] The $Co_{98.5}Ru_{1.5}$ composition was identified by DFT calculations as one of the most promising candidates among 348 screened bimetallic catalyst nanoalloys for the amination of octan-1-ol using ammonia. This was further validated by experiments.[27] Co and Ru can also be associated to achieve catalysts with a better activity towards water splitting[28] or towards hydrolysis of ammonia borane[29] due to induced lattice strains which modulate the electronic structure. Moreover, the addition of Co to Ru can

[a] *Université Paris Cité, CNRS, ITODYS, F-75013 Paris, France. E-mail: lorette.sicard@u-paris.fr, jean-yves.piquemal@u-paris.fr*
[b] *Université de Toulouse, Laboratoire de Physique et Chimie des Nano-Objets, UMR 5215 INSA, CNRS, UPS, 135 Avenue de Rangueil, F-31077 Toulouse, cedex 4, France*
[c] *Graduate School of Environmental Studies, Tohoku University, Sendai 980-8579, Japan*
[d] *Laboratoire Interdisciplinaire sur l'Organisation Nanométrique et Supramoléculaire, Université Paris Saclay, NIMBE UMR 3685 CEA-CNRS, 91191 Gif sur Yvette, France*
[e] *Synchrotron SOLEIL, L'Orme des Merisiers, Départementale 128, 91190 Saint-Aubin, France*

† Electronic supplementary information (ESI) available. See DOI: https://doi.org/10.1039/d3cp02522e

result in the emergence of magnetic properties[30] which is valuable for recovering unsupported nanocatalysts. Recently, we also demonstrated that the addition of a small quantity of a noble metal such as Ru ([Ru]/[Ru + Co] = 2.5 mol%) was mandatory for the formation of monodisperse Co nanorods with controlled shapes in polyol medium. A Ru nucleus was found at the exact center of each nanorod, demonstrating the role of Ru as a nucleating agent. Depending on the reaction conditions, Ru NPs could also be present at the particle surface.[31,32] These Co nanorods are very active towards the acceptor-less dehydrogenation of primary alcohols and show better catalytic stability during recycling than nanorods which are not decorated with Ru.

We also recently evidenced that Co_xRu_{100-x} alloy nanoplatelets show better catalytic activity towards the acceptor-less dehydrogenation of alcohols than their monometallic counterparts.[33] The synthetic method consisted in co-reducing acetylacetonate Co(II) and Ru(III) precursors in octan-1-ol at the boiling point. Co and Ru are theoretically miscible elements in the bulk state.[34] In a first approximation, metal ions displaying similar redox potential are more likely to form an alloy. Yet, this is not the case for Co and Ru ($E^0(Ru^{3+}/Ru)$ = 0.39 V *vs.* SHE) and $E^0(Co^{2+}/Co)$ = −0.28 V *vs.* SHE).[35] Although redox potential values can serve as a guide to assess the reducibility of metal species, they are given under standard conditions (25 °C and 1 atm), conditions that differ significantly from those used in the synthesis. Moreover, ligands coordinated to the metal center also influence the redox potential value and the solvent potential plays a role in the kinetics of reduction.[11] Depending on the solvent and metal salt precursor, we obtained either bimetallic nanoparticles or a mixture of monometallic ones.[33] The formation of homogeneous structures necessitates either the simultaneous reduction of the two metal ions which nucleate and grow together to generate alloy nanocrystals,[11,36] the formation of a core shell structure followed by interdiffusion or a dissolution-reprecipitation process. Understanding the reaction pathway and the key parameters controlling the atomic arrangement (leading either to segregation or mixing) is of outmost importance to tailor NPs with tunable properties. For this purpose, we have studied the kinetics of reduction of the ions, taken either separately or together to assess the possible influence of one metal on the other and the nature of the intermediate species formed during the reaction. The three compositions previously published (Co_xRu_{100-x} with x = 20, 50 and 80) were studied to assess whether the ratio of Co to Ru had an influence on the reduction pathway and intermediate species which could form. Different complementary techniques have been used to follow the reaction: UV-visible spectroscopy, *in situ* X-ray Absorption Fine Structure (XAFS), Small angle X-ray scattering (SAXS) and H_2 flow metering (molecular hydrogen being generated as a side product during the reaction). The observation of the species and of their reduction *in situ* is critical as the intermediate species that form at a given temperature can be metastable and transform when freezing aliquots to analyze them at ambient temperature. The combination of all these data provides a thorough understanding of the influence of one metal on the reduction pathway of the other one and leads to the proposition of a formation mechanism for the nanoalloys.

2. Experimental

2.1. Chemicals

Ru acetylacetonate, $Ru(acac)_3$, (Alfa Aesar, 97%), Na acetylacetonate monohydrate, $Na(acac)\cdot H_2O$, (Sigma Aldrich, 97%) and octan-1-ol (AlfaAesar, >99%) were used as purchased. Co acetylacetonate, $Co(acac)_2$, (Sigma Aldrich, 97%) was dried in an oven for at least one night at 50 °C before use.

2.2. *Ex situ* synthesis

The preparation of the Co_xRu_{100-x} samples has been reported elsewhere.[33] Briefly, $Ru(acac)_3$ and $Co(acac)_2$ are dissolved at room temperature (RT) in octan-1-ol with the targeted molar ratio and a global metallic concentration of 16.3 mmol L^{-1} and flushed with Ar. The solution was then heated up to the boiling point, *ca.* 190 °C, at a rate of 10 °C min^{-1}. After 90 minutes under reflux, the solution is cooled down to RT. The nanoparticles are recovered by centrifugation at 20 000 rpm and washed twice with absolute ethanol and once with acetone.

2.3. Characterization techniques

UV-Visible spectra were recorded on a PerkinElmer Lambda 1050 spectrometer equipped with a three-detectors module to work in the 175–3300 nm wavelength domain. The spectra were recorded using a quartz Suprasil™ demountable cell with an optical path length of 0.2 mm. The kinetics of reduction of Ru(III) was followed by this technique for solutions containing (i) 16.3 mM of $Ru(acac)_3$ and (ii) 8.15 mM of both $Ru(acac)_3$ and $Co(acac)_2$ in octan-1-ol. For this purpose, aliquots were taken every 10 °C during the heating ramp and at different times of the stage at 190 °C.

The oxidation state and the local environment of metal species in the precursor solutions of Ru, Co_xRu_{100-x} (x = 20, 50 and 80) and Co have been followed *in situ* during the heating ramp from RT to the boiling temperature by time-resolved X-ray absorption spectroscopy at SOLEIL Synchrotron facility on the Quick-EXAFS ROCK beamline using a specially designed PEEK cell (see Fig. S2, ESI†). The dimension of the cell has been optimized for recording Quick-EXAFS spectra at the Co K edge (Optical Path (OP) = 0.6 cm) and at the Ru K edge (OP = 8 cm) for the same solution. For this purpose, the cell installed on the motorized rotation stage is rotated to align either along the short OP or the long one to the X-rays beam for data collection in transmission mode. More details on the PEEK cell and sample environment used for the *in situ* Quick-EXAFS monitoring are given in the ESI† Section S2.1.

The heating rate of 10 °C min^{-1} up to the boiling temperature, as for the *ex situ* experiments, gave a non-satisfactory signal to noise ratio. Consequently, the temperature was raised stepwise with a lower average heating rate of 5 °C min^{-1}. Moreover, the boiling temperature of the solution is close to 190 °C but the setup did not permit it to stay for a long time at

this temperature as a cooling system limited the evaporation of the solvent but did not prevent it completely. The plateau was thus set at 180 °C instead of 190 °C. As only the data recorded during the heating step were further processed, this is not an issue. The heating profile is given in Fig. S3 (ESI†). The beamline permits the so-called edge jumping:[37] Si(111) and Si(220) Quick-EXAFS monochromators together with the respective B_4C and Pd harmonic rejection mirror stripes are exchanged in less than 35 s for recording Co and Ru K edge data, respectively. Nevertheless, *in situ* monitoring of thermal treatments for bimetallic systems were carried out independently at the Ru and Co K edges. Following only one edge allows us to obtain more spectra within a short period of time. At the end of the reactions, spectra at both edges were recorded using the edge jumping to ensure the reproducibility of the reactions by checking that similar results were obtained at both edges. For measurements of NPs produced *ex situ*, the pellets were prepared by carefully mixing the as-prepared powders with boron nitride (weight ratio of NPs to BN of *ca.* 1 : 2 and 1 : 5 for Ru and $Co_{80}Ru_{20}$, respectively). Before recording the XAS data, a scan of the sample in x and y orthogonal directions was carried out at a fixed monochromator energy in order to check the pellet homogeneity. Pellets from $Ru(acac)_3$ and $Co(acac)_2$ powders were also prepared following this procedure and the spectra recorded were used as references in addition to a Co foil. Finally, the Co K edge spectrum of CoO used as a reference was that obtained in a previous work by heating Co_3O_4 crystallites dispersed on alumina under a H_2 flow at 500 °C.[38]

Ionization chambers filled with N_2 and a mixture of N_2 and Ar were used for measuring the intensities of photons at the Co and Ru K edges, respectively. A Co foil (E_0 = 7709 eV) and a RuO_2 pellet (E_0 = 22135.6 eV) previously calibrated on a Rh foil (E_0 = 23 220 eV) were measured simultaneously to the sample spectra with a third ionization chamber for energy calibration. The typical time resolution for kinetic monitoring was 10 s corresponding to the merging of 20 consecutive recorded Quick-EXAFS spectra, each being acquired at 2 Hz oscillation frequency of the Quick-EXAFS monochromators (250 ms per spectrum with ascending Bragg angles).

The spectra were normalized using the graphic interface *normal_gui*[39] written in Python and dedicated to spectra measured on ROCK for a massive and quick normalization allowing the reconstruction of a matrix of experience. Multivariate-Curve Resolution with Alternative-Least Squares (MCR-ALS) methodology[40] using the MCR-ALS gui 2.0 developed by R. Tauler *et al.* on the Matlab® platform[41] was used for isolating from the experience matrix the concentration profiles of the species participating to the reaction and their associated XAS spectra. The use of MCR-ALS applied for XAS analysis is extensively described in the literature.[42–45] The analysis of the spectra was performed using Demeter (Athena and Artemis programs).[46]

The SAXS data were acquired on a homemade laboratory instrument with a Mo X-ray generator.[47] The samples were recorded in a cell with Kapton windows in the q range from 0.01 to 0.2 $Å^{-1}$. Calibration of the q range was performed using dodecanol while the absolute intensity was obtained using a Lupolen standard. Analysis of the data was performed using Sasview free software.[48]

The evolution of H_2 during particle synthesis was measured using a Bronkhorst flowmeter linked to a micro-computer. Considering the acceptor-less dehydrogenation mechanism for octan-1-ol: $C_7H_{15}CH_2OH = C_7H_{15}CHO + H_2$, conversion of the alcohol can be calculated by measuring the volume of generated H_2, assuming that the perfect gas law is verified.

3. Results

The nanoalloys were prepared using a simple soft chemistry route relying on the use of a long-chain alcohol that has a dual role: the solvent and a mild reducing agent allowing the reduction of Co(II) and Ru(III) species into their zero-valent state (see Fig. 1a). The obtained particles correspond to hexagonal platelets (see Fig. 1b–d) and HAADF-STEM coupled to EDX analyses reveals the formation of alloys as reported in a previous study.[33] In contrast, large aggregates are isolated for pure Co and nanoflowers corresponding to the agglomeration of particles with a size of a few nanometers were obtained for pure Ru (see Fig. 1e and f). Clearly, the combination of the two metals allows for the formation of Co_xRu_{100-x} particles with well-defined morphologies but the reaction mechanism has to be clarified.

3.1. UV-visible spectroscopy

First, UV-visible characterization was carried out to quantitatively follow the reduction of the metal species. The spectra of Na(acac), $Co(acac)_2$ and $Ru(acac)_3$ and the peak attributions are given in Fig. S1 and Table S1 in the ESI.† For the $Co(acac)_2$ complex, only the transitions of the solvent and the $\pi \rightarrow \pi^*$ transition of the acac ligand are visible. Spin-allowed but Laporte-forbidden transitions are normally expected but are not seen easily because the molar absorption coefficient values are well lower than those associated with spin- and Laporte-allowed electronic transitions.[49] Consequently, the kinetics or reduction of Co(II) could not be monitored by this technique. On the contrary, for the $Ru(acac)_3$ complex, three peaks with a high molar absorption coefficient are detected (see the ESI,† Section S1), as already reported.[50] Aside from the transition at 271 nm associated with the acac ligand, two other peaks due to metal to ligand or ligand to metal charge transfer transitions are visible at 349 and 506 nm. The UV-visible spectra of an equimolar solution of $Ru(acac)_3$ and $Co(acac)_2$ in octan-1-ol collected during the rise and at the plateau at the final temperature are given in Fig. 2a. A clear evolution is observed: with reaction time, the intensity of the two charge transfer peaks decreases until disappearing while that of the peak at 271 nm, attributed to the acac ligand, decreases to a much lower extent. The Ru(III) concentration was deduced from the absorbance value of the peak at 506 nm, using the Beer–Lambert law and the molar extinction coefficient determined previously (see Table S1, ESI†).

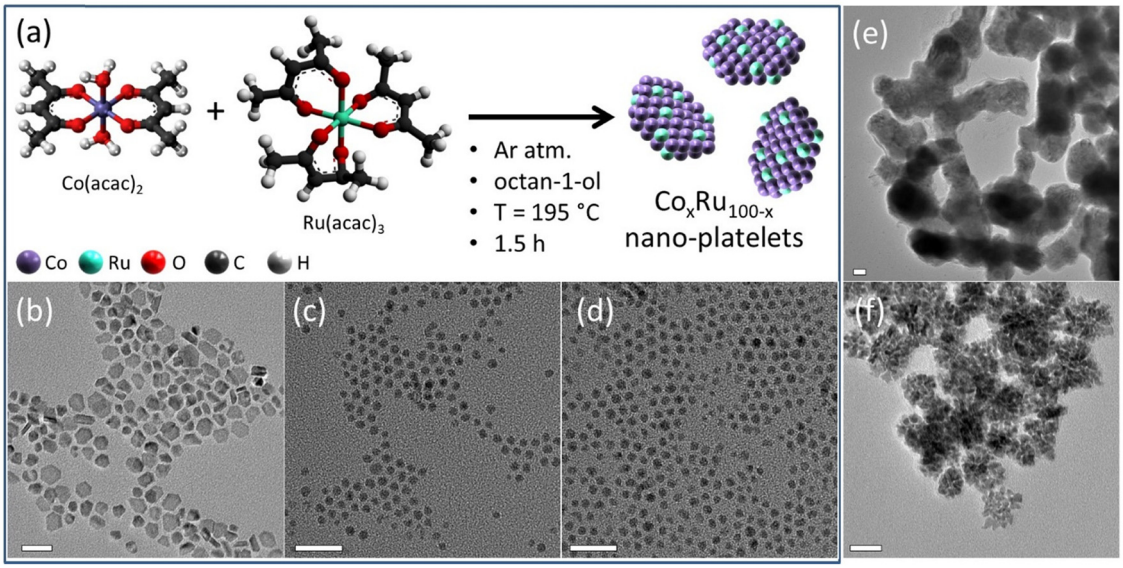

Fig. 1 (a) Synthetic scheme for the formation of the Co_xRu_{100-x} nanoalloys and TEM images of (b) $Co_{80}Ru_{20}$, (c) $Co_{50}Ru_{50}$, (d) $Co_{20}Ru_{80}$, (e) pure Co and (f) pure Ru samples. The scale bar corresponds to 20 nm.

The temporal evolution of the Ru(III) concentration for two reactive solutions, $Ru(acac)_3$ in octanol and an equimolar mixture of $Ru(acac)_3$ and $Co(acac)_2$, are given in Fig. 2b. At 80 °C, the Ru(III) concentration for these two solutions is close to the theoretical values of 16.3 and 8.15 mM for Ru and $Co_{50}Ru_{50}$, respectively. The evolution is very similar for the two systems: a similar sharp decrease in the Ru concentration with time is observed after *ca.* 16–17 minutes (170–185 °C temperature range). This clearly evidences that the presence of Co(II) species does not influence the kinetics of reduction of Ru(III).

UV-visible spectroscopy gave a good insight into Ru(III) reduction but provided no information on the reduction of Co(II) species. Thus, *in situ* X-ray Absorption Spectroscopy (XAS) experiments at the Ru and Co K-edges were carried out to accurately study the kinetics of metallic ion reduction taken separately or together.

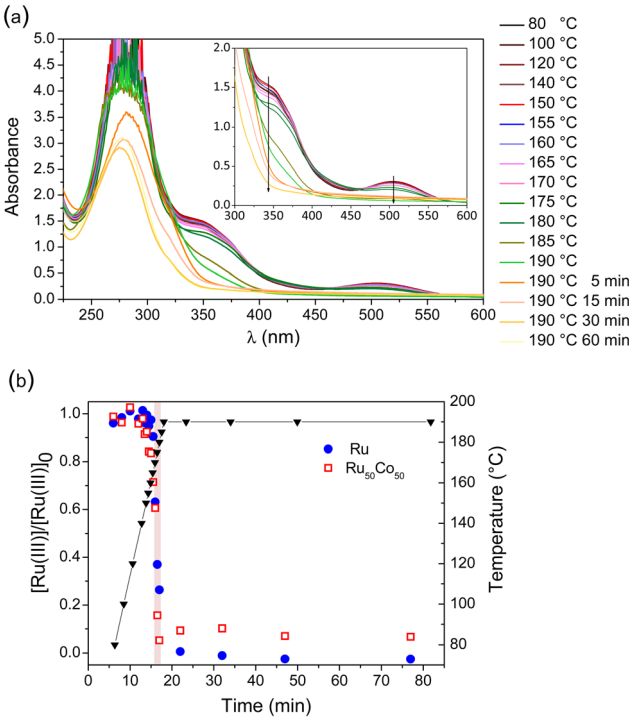

Fig. 2 (a) UV-visible spectra obtained during heating an equimolar solution of $Ru(acac)_3$ and $Co(acac)_2$ in octan-1-ol. Inset: Magnification in the 300–600 nm range. (b) Evolution of the relative Ru(III) concentration during the synthesis of Ru (●) and $Co_{50}Ru_{50}$ (□) NPs deduced from the absorbance value at 506 nm and associated temperatures (▼) at which the aliquots were taken.

3.2. X-Ray absorption spectroscopy (XAS)

3.2a Kinetics of the reduction of Ru(III) species. The XAS spectrum at the Ru K edge of the $Ru(acac)_3$ powder and of the $Co_{20}Ru_{80}$ precursor solution before heating (Room Temperature) and after *in situ* heating for 15 min at the boiling temperature and cooling (after cooling) are plotted in Fig. 3. The spectra of the $Ru(acac)_3$ powder and of the solution before heating are similar, indicating that no reduction of Ru(III) species has occurred at room temperature in octan-1-ol nor modification of the Ru environment. The spectrum of the solution obtained after heating for 15 minutes at the boiling point and cooled down to room temperature is very similar to that of Ru(0) foil.[51] The edge is shifted towards a lower energy compared to the previous spectra, indicating the reduction of Ru(III) during the heating stage. The shift in energy is maximum at a normalized absorbance of *ca.* 0.3 (see the inset in Fig. 3). Consequently, this energy value will be further used to follow the reduction of Ru species.

The precursor solutions with the Ru, $Co_{20}Ru_{80}$, $Co_{50}Ru_{50}$ and $Co_{80}Ru_{20}$ compositions were all analyzed by XAS at the Ru K-edge *in situ* during the heating ramp using the afore-mentioned specific cell designed for this study (see Section S2 in the ESI†). The results are displayed in Fig. S4 (ESI†). The quantitative

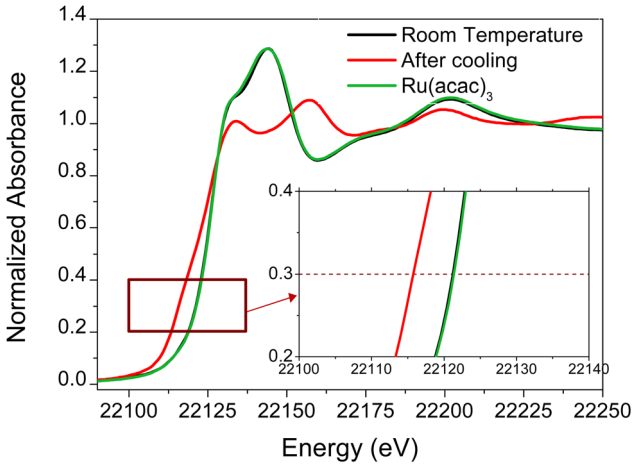

Fig. 3 Normalized XAS spectra of the $Co_{20}Ru_{80}$ reactive solution at the Ru K edge (at room temperature and after cooling) and of the $Ru(acac)_3$ powder. The inset is an enlargement of the plot to show the difference of the energy value at a normalized absorbance of 0.3.

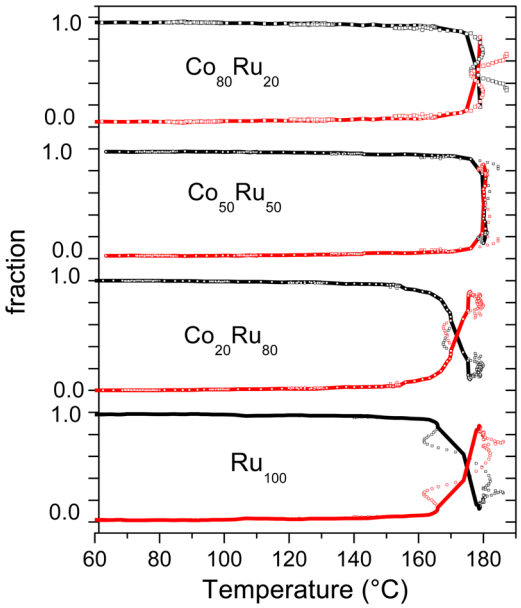

Fig. 4 Evolution of the molar fraction of the Ru(III) (in black) and Ru(0) (in red) species during the heating ramp for the precursor solutions of (a) $Co_{80}Ru_{20}$, (b) $Co_{50}Ru_{50}$, (c) $Co_{20}Ru_{80}$, and (d) Ru. The points are the experimental data whereas the lines give the evolution profile.

evolutions of both the edge at 0.3 normalized absorbance and white line intensity are given in Fig. S5 and S6 (ESI†), respectively. A similar evolution is observed for all the solutions, irrespective of the Co concentration. First, both the rising edge position and the white line intensity at *ca.* 22148.5 eV remain nearly invariant until the temperature of the solution gets close to the boiling temperature, *i.e. ca.* 160–170 °C. Second, the position of the edge at 0.3 normalized absorbance shifts abruptly towards a lower energy as the reaction proceeded to higher temperatures whereas the white line intensity decreases concomitantly, indicating a decrease of the oxidation state of Ru at the end of the heating ramp.

Owing to the high number of spectra obtained with Quick-EXAFS, chemometric analysis was carried out, using a combination of Principal Component Analysis (PCA) and Multivariate Curve Resolution with Alternating Least Squares (MCR-ALS) methods, which are detailed in the ESI† (Section S2.2). The latter method is particularly powerful for solving the mixture problem by isolating, from time-resolved spectroscopic data sets obeying the Beer–Lambert law, the spectra of pure species and their corresponding concentration profiles.[40] Irrespective of the solution composition, the PCA analysis indicates that only two Ru species are present in our system. No intermediate species were identified. Common spectra of the two species for the four sets of data were obtained using a Column-Wise matrix Augmentation (CWA) strategy (see the ESI†). They are shown in Fig. S7 (ESI†). The spectrum of the first Ru(III) species is similar to the one of the $Ru(acac)_3$ solution while the second one, characteristic of metallic Ru, is slightly different from the last ones obtained *in situ* because the reduction is not totally achieved after 15 minutes heating at the boiling temperature. These latter can be reconstructed by a combination of the spectra of the first and second pure species obtained by MCR-ALS as shown in Fig. S8 (ESI†).

The evolutions of the fraction of Ru(III) and Ru(0) species as a function of temperature for the four compositions are given in Fig. 4. The profiles of the four solutions are similar and strongly related to the previously shown evolution of the rising edge position at 0.3 (normalized absorbance) and white line intensity (Fig. S5 and S6, ESI†). A quick reduction of Ru(III) to Ru(0) is observed near the boiling temperature, from 160 °C for the Ru rich compositions and 170 °C for the Co rich ones. It is reminded that the heating ramp was not linear with temperature oscillations due to overshooting, giving the non-monotonous evolution. During this step of quick evolution of the Ru species (160 °C to boiling temperature), a small decrease in temperature does not completely stop the reduction but rather slows it down. However, the general profile drawn in Fig. 4 is very similar to that obtained by UV and can thus be relied on.

From the above results, three important conclusions can be drawn: (i) the evolution described here is similar to that already observed by UV-visible spectroscopy; the slight differences in reduction temperature are explained by the different ramping rates used for EXAFS (5 °C min^{-1}) and for UV-visible spectroscopy experiments (10 °C min^{-1}); (ii) the presence of Co in the system has a very limited impact on the reduction kinetics of Ru(III) and (iii) the reduction of Ru(III) to Ru(0) occurs directly, without the formation of any intermediate species.

The recovered solids (after 1 h 30 heating under reflux) have also been characterized by EXAFS. Fig. S9 (ESI†) shows the Ru EXAFS Fourier transformed moduli while Table 1 gives the fitted parameters for pure Ru and the powder containing 20% Ru. For both samples, the number of O neighbouring atoms is close to 1, indicating a limited oxidation of Ru, probably at the surface. The number of Ru neighbours in the first shell of pure Ru NPs is similar to that found by G. Viau *et al.*[52] for 1.9 nm particles synthesized in polyol. For random distribution of

Table 1 EXAFS fitting parameters at the Ru K-edge for the spectra of Ru and $Co_{80}Ru_{20}$ powders obtained in the laboratory (S_0^2 = 0.9; E_0 = 22130.0 eV. The fits were made between R = 1 and 3 Å; from k = 4 to 16 $Å^{-1}$ with dk = 2 (Kaiser Bessel)

Backscatter	N	R (Å)	σ^2 ($Å^2$) × 10^3
Ru NPs			
Ru	8.4 ± 0.6	2.68 ± 0.01	6 ± 1
O	0.9 ± 0.4	1.96 ± 0.01	11 ± 4
r-factor = 0.0063	X^2 = 481; X_{red}^2 = 43.7	N_{ind} = 17	N_{var} = 6
$Co_{80}Ru_{20}$ NPs			
Ru	5.2 ± 0.2	2.65 ± 0.01	6 ± 1
Co	4.6 ± 1.3	2.59 ± 0.02	11 ± 1
O	1.3 ± 0.2	1.97 ± 0.01	12 ± 2
r-factor = 0.003	X^2 = 46; X_{red}^2 = 5.75	N_{ind} = 17	N_{var} = 9

r-factor: overall fit quality factor, X^2 (X_{red}^2): (reduced) chi-square goodness-of-fit test, N_{ind}: maximum number of independent points in the data, N_{var}: number of variables in the fit.

cobalt and ruthenium in the $Co_{80}Ru_{20}$ alloyed sample, 4 more Co neighbours than Ru ones should be found. Herein the best simulation indicates a nearly equal number of Co and Ru as first neighbours (a constrain of 4 more Co than Ru leads to an r-factor of 0.024, far higher than the one found by refining the two numbers of neighbours independently). This suggests that the particles are not totally homogeneous, in line with previously published results.[33] This will be further discussed when analyzing the EXAFS data at the Co K-edge.

3.2b Kinetics of the reduction of Co(II) species. A solution of $Co(acac)_2$ alone in octan-1-ol as well as the solutions containing $Co(acac)_2$ and $Ru(acac)_3$ in different proportions were also analyzed by *in situ* XAS at the Co K-edge upon heating. The obtained spectra are given in Fig. 5 for Co and $Co_{80}Ru_{20}$ solutions and Fig. S10 (ESI†) for all the compositions. The evolutions, as the temperature rises, of the energy for a normalized absorbance of 0.3 and of the white line intensity are given in Fig. S11 and S12 (ESI†), respectively. The spectra are similar for all the compositions at the beginning but the evolution differs between the solution containing Co cations only and those also containing Ru cations. In the first case, only a slight decrease in the white line intensity and a slight continuous decrease of less than 2 eV of its energy position are observed during the heating step and for the first minutes at the boiling temperature (see Fig. S11 and S12, ESI†). The absence of a significant variation in energy of the rising edge indicates that no modification of the cobalt oxidation state occurs. In the presence of Ru, the intensity of the white line decreases much more and the shoulder in the rising edge is much more marked (Fig. 5b). The shape of the spectra in the solutions containing ruthenium after heating is characteristic of a Co(0) species and, for those solutions, a 2-step process is observed. From RT to *ca.* 160 °C, only the white line significantly decreases in intensity from *ca.* 1.6 to 1.4 with no marked change in the rising edge position, whereas an abrupt shift of edge position and of the white line intensity occurs above 160 °C to the values characteristic of metallic cobalt. These findings clearly indicate that Ru triggers Co(II) reduction.

Thus, the *in situ* Co K-edge XAS monitoring of the reaction clearly evidences that for pure Co, the reduction of Co(II) cations has not occurred after heating for about 15 min at the boiling temperature (and subsequent cooling) contrary to what happens when adding Ru species. This can be seen in Fig. S13 (ESI†) where the obtained spectrum is very close to that of the CoO reference. However, it is possible to reduce it to metallic Co if the reaction proceeds for a longer time, typically 1 h 30.

The data of the solution containing only $Co(acac)_2$ was first analyzed. The PCA method was used to determine the number of species formed during heating. A set of 3 species has to be considered to account for the observed experimental data (see Fig. S14, ESI†). The spectra of species obtained by MCR-ALS are given in Fig. 6a and their EXAFS signals in Fig. S15 (ESI†). The evolution of each of these species during heating is plotted in Fig. 6b. Note that the spectrum at the Co K-edge for the powder obtained for 1 h 30 at 190 °C is also presented as A4 in Fig. 6a. In this manner, a complete picture of the different species generated during the course of the reaction can be obtained. The spectrum of the first Co pure species in octan-1-ol before

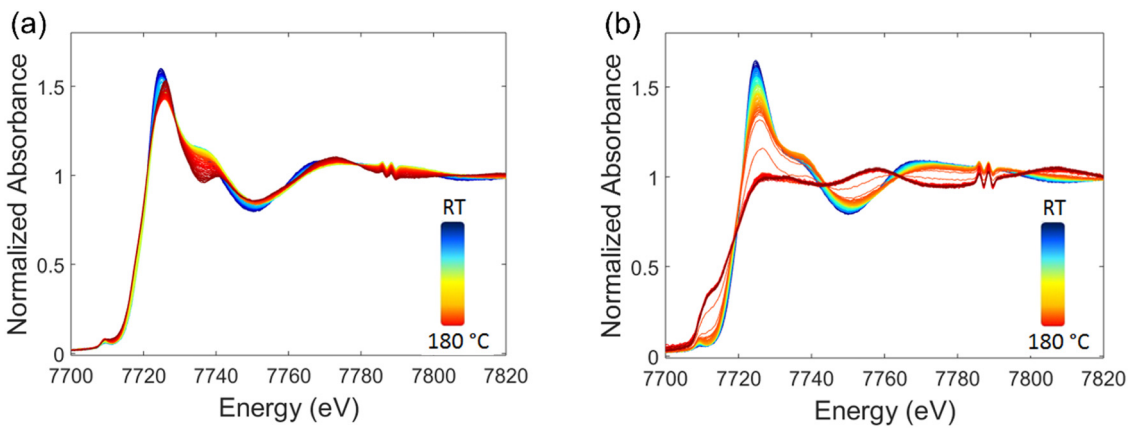

Fig. 5 Normalized spectra at the Co K-edge obtained when heating the precursor solutions of Co (a) and $Co_{80}Ru_{20}$ (b) NPs (the colour evolves from blue at room temperature to red at 180 °C).

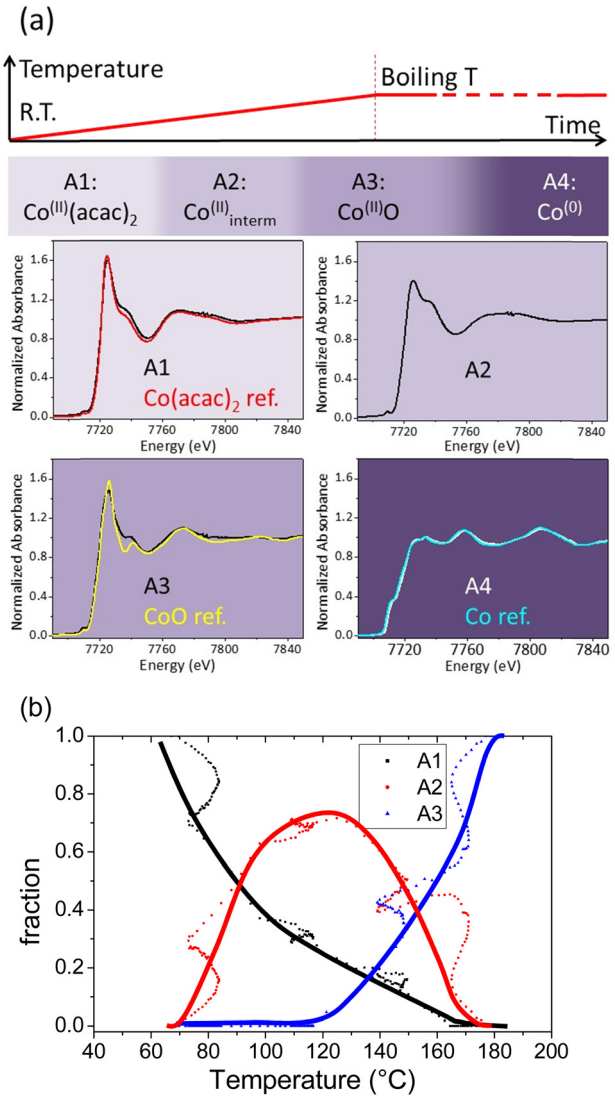

Fig. 6 (a) Spectra at the Co K-edge of the species A1, A2 and A3 extracted with the MCR-ALS method during heating a solution of $Co(acac)_2$ in octan-1-ol and of the powder (A4) obtained after 1 h 30 heating at the boiling temperature. Spectra at the Co K-edge of the $Co(acac)_2$, CoO and Co references are also given for comparison purposes. (b) Speciation diagram for the A1, A2 and A3 species as a function of temperature. The points are experimental data and the lines give the general tendency.

heating (at RT), denoted A1, is nearly identical to that of the $Co(acac)_2$ solid precursor. As for pure $Ru(acac)_3$, this shows that there is no reduction of Co(II) at RT (*vide supra*) and no significant modification of the Co environment. Next, an intermediate A2 species appears at 70 °C and predominates at 90 °C. The X-ray absorption spectrum of A2 differs from the $Co(acac)_2$ and CoO references. The distance between Co and the O in the first shell is decreased by *ca.* 0.1 Å compared to that obtained for A1 (see Fig. S15b, ESI†). We assume that, during heating, there is a partial replacement of acac ligands by octan-1-ol molecules in the first coordination sphere of the Co(II) metal center or formation of polymeric species of Co(II) acetylacetonate. Then, a third species (A3) is generated between 120 and 160 °C and it is the only Co-containing species present when reaching the boiling temperature. Its X-ray absorption spectrum at the Co K-edge is close to that of the 500 °C-H_2 as-prepared CoO reference (see Fig. 6). EXAFS oscillations for both spectra are clearly in phase and amplitude differences are ascribed to different particle sizes and Debye–Waller factors between both samples (see Fig. S15a, ESI†). The similarity between the FT moduli of A3 and CoO can also be seen in Fig. S15c (ESI†). The powder obtained after 1 h 30 heating under reflux (species A4) is then similar to the Co(0) reference.

The key result is that, without Ru and for a reaction time of a few minutes at the boiling temperature, the reaction ends with the formation of a CoO-like phase while reduction of Co(II) to Co(0) has not occurred. During the 1 h 30 stage at the boiling temperature, the CoO phase transforms into metal Co, following a mechanism which is not in the scope of this study.

MCR-ALS treatment (see Fig. S16, ESI†) was similarly carried out for the Co_xRu_{100-x} bimetallic particles (x = 20, 50, 80). Three components (including the initial species) were also deduced. They are called B1, B2 and B3 (see Fig. 7a and Fig. S15, ESI†). The first MCR-ALS species are similar irrespective of the Co to Ru ratio, including pure Co, *i.e.* A1 and B1 are similar. Regarding the 2nd species, the spectra isolated for $Co_{80}Ru_{20}$, $Co_{50}Ru_{50}$ and $Co_{20}Ru_{80}$ are superimposable and in close relationship with the one isolated for the pure Co composition indicating that a common cobalt intermediate species is formed irrespective of the ruthenium content. In other words, it means that species A2 and B2 are close and probably correspond to Co centers with a partial replacement of acac ligands by octan-1-ol molecules or the formation of clusters, as proposed above. A very noticeable result is that species B3 differs strongly from species A3 (without Ru). In the case of pure Co, A3 is close to CoO and reduction to Co(0) necessitates much more than 15 min at the boiling temperature whereas for Co_xRu_{100-x} alloys, B3 is characteristic of metallic Co as displayed in Fig. 7 and Fig. S15 (ESI†). The slight differences in the shape of the XANES spectra for $Co_{80}Ru_{20}$, $Co_{50}Ru_{50}$, $Co_{20}Ru_{80}$ and Co foil is ascribed to the replacement of cobalt by ruthenium.

The Co speciation diagram for the $Co_{80}Ru_{20}$ sample is given in Fig. 7b and in Fig. S17 (ESI†), together with those of the $Co_{50}Ru_{50}$ and $Co_{20}Ru_{80}$ materials. They are very similar for the bimetallic samples irrespective of the Co to Ru ratio. However, they are also very different from that obtained for pure Co (Fig. 6a). For bimetallic particles, the initial species disappears progressively between 70 and 150 °C whereas the intermediate species 2 appears. It is interesting to note that this intermediate species B2 does not evolve towards CoO and is, on the contrary, stable in the temperature range at which CoO forms for pure Co (T > 120 °C). B2 then transforms into Co(0) between 160 °C and the boiling temperature, the same range observed for the reduction of Ru in our system. This effect of Ru as a promotor of the reduction of Co is well known in the preparation of catalysts used for the Fischer Tropsch reaction.[53] Small angle X-ray scattering (SAXS) experiments carried out on aliquots confirmed the formation of particles in this range (see S3 in the ESI†).

The fitting parameters for the $Co_{80}Ru_{20}$ powder are given in Table 2 (see Fig. S18 for the fits, ESI†). Co atoms have in majority Co atoms in their first coordination shell. The EXAFS

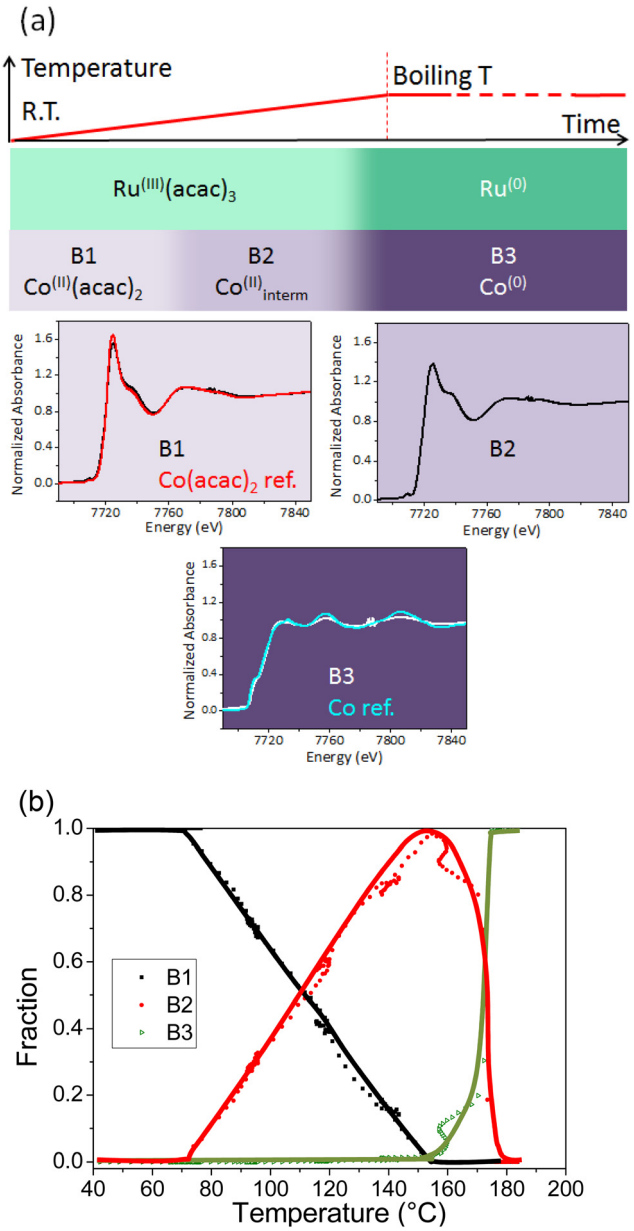

Fig. 7 (a) Spectra at the Co K-edge of the species B1, B2 and B3 extracted with the MCR-ALS method during heating a solution of $Co(acac)_2$ and $Ru(acac)_3$ in octan-1-ol for the $Co_{80}Ru_{20}$ composition. Spectra at the Co K-edge of the $Co(acac)_2$ and Co references are also given for comparison purposes. (b) Speciation diagram for the B1, B2 and B3 species as a function of temperature, tendency extracted from Fig. S20 (ESI†).

fitting parameters of the $Co_{80}Ru_{20}$ establish that Ru atoms are surrounded by as much Ru as Co atoms and that Co atoms are surrounded by 17.5 more atoms of Co compared with Ru, which is much more than the expected 4 to 1 stoichiometry. This means that Co and Ru are not homogeneously distributed throughout the sample. This confirms the results reported in a previous paper[33] which enlightened the presence of platelets of two different compositions $Co_{50}Ru_{50}$ and $Co_{86}Ru_{14}$. O atoms are also found. The powder is thus partly oxidized as shown by XPS.[33]

Table 2 EXAFS fitting parameters at the Co K-edge for the spectra of the $Co_{80}Ru_{20}$ powder obtained in the laboratory. $S_0^2 = 0.86$; $E_0 = 7716.6$ eV. The fits were made between $R = 1$ and 3 Å; from $k = 4.4$ to 10.8 $Å^{-1}$ with $dk = 2$ (Kaiser Bessel)

Backscatter	N	R (Å)	σ^2 ($Å^2$) × 10^3
$Co_{80}Ru_{20}$ NPs			
Ru	0.4 ± 0.8	2.58 ± 0.01	9 ± 4
Co	7.0 ± 0.6	2.50 ± 0.03	7 ± 1
O	1.2 ± 0.9	2.00 ± 0.04	15 ± 5
r-factor = 0.003	$X^2 = 928$; $X_{red}^2 = 185$	$N_{ind} = 10$	$N_{var} = 5$

3.3. Gas phase evolution

When heating the reactive solution to the boiling temperature, the formation of gas was observed. The formation of H_2 was attested by micro-GC (see Fig. S22a and Section S4 in the ESI†). Its evolution was monitored with a gas flow meter during the synthesis of the different Co_xRu_{100-x} compounds. The instantaneous hydrogen flow is plotted in Fig. 8a and the calculated conversion (see the experimental part for details) in Fig. 8b. During heating, H_2 formation is observed from *ca.* 170 °C

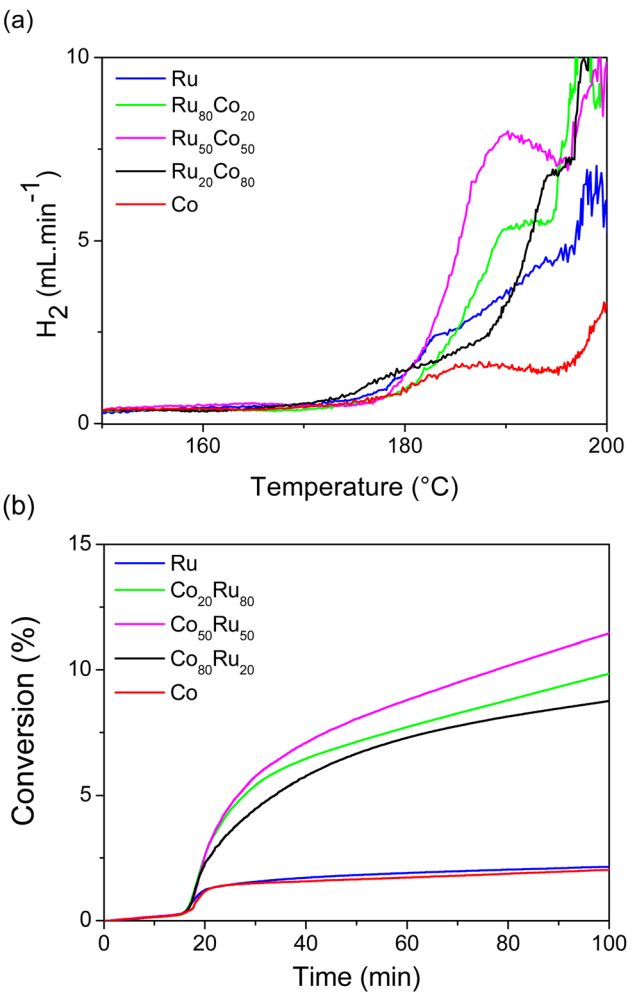

Fig. 8 (a) Instantaneous H_2 flow measured during the synthesis of the Co_xRu_{100-x} NPs and (b) calculated octan-1-ol conversion using the total volume of evolved H_2.

(corresponding to *ca.* 17 min reaction time with the ramping rate used), irrespective of the Ru composition studied, confirming that the reduction of the metal species begins at this same temperature for all the samples. The quantity of H_2 formed at 190 °C (see Fig. 8a) is the lowest for Co only and the highest for the $Co_{50}Ru_{50}$ composition. After this reduction stage, the formed nanoparticles catalyze the conversion of octan-1-ol mainly into octanal (see Fig. S22b, ESI†), giving a second rise in the H_2 formation plot. The nanoalloys were found to be better catalysts for this reaction than pure Co or Ru (see Fig. 8a) as already demonstrated for octan-2-ol[33] even if conversion and selectivity were lower for the primary alcohol than for the secondary one.

4. Discussion

The results obtained clearly establish that the addition of Co(II) to a solution of Ru(III) does not influence much the kinetics of reduction of Ru(III) which occurs between 160 and 180 °C as demonstrated by UV-visible and X-ray absorption spectroscopies. On the contrary, the presence of Ru(III) favors the reduction of Co(II), whatever the Ru(III) atomic percentage between 20 and 80%. Indeed, a co-reduction of Co(II) and Ru(III) is observed in the 160–180 °C range for mixed solutions whereas the precipitation of solid CoO (as attested by EXAFS and SAXS) is observed in this same temperature range for pure Co solutions. In this monometallic solution, the reduction of CoO requires a prolonged reaction time at the boiling temperature. It is noteworthy that CoO is not identified as an intermediate species when Ru(III) is added.

The effect of noble metals such as Ru as a promoter of the reduction of Co(II) is well known and widely used in heterogeneous catalysis where noble metals in very small amounts (Ru/Co $<$ 0.08 at.) are often added to prepare Co-based Fisher Tropsch catalysts.[54] Even if the reduction conditions are very different for these catalysts (thermal treatment of metal species on oxide substrates), Ru was shown to enhance the reducibility of Co_3O_4 to CoO and that of CoO to Co as well as to decrease the average Co cluster size,[53] which is in line with our results. CoO was not identified as an intermediate species but Ru may promote the reduction of the Co(II) species B2 or CoO might form as a transient species within a too short time scale and/or too small quantity to be observed. Other studies showed that the reduction of Ru(IV) impregnated on Co_3O_4 resulted in the concomitant formation of CoO and Ru(III) further reduced into Ru(0) at the surface of CoO nanoparticles enabling hydrogen activation for the further reduction of Ru/CoO species to the metallic state in an autocatalytic process.[45] It was also reported that reducing Ru complexes in a basic polyol medium involves the formation of molecular ruthenium hydrides which decompose to form Ru clusters with molecular dihydrogen release.[54,55] The formation of Co nanorods from $Co(laurate)_2$ in 1,2-butanediol in the presence of Ru(III) cations was also shown to proceed in two steps both involving the release of H_2.[31] In this study, the first H_2 production event at 150 °C was associated with the reduction of Ru(III) through the decomposition of hydrides formed *in situ* and the second one to the catalytic dehydrogenation of the polyol solvent by the formed Co nanorods. The evolution of H_2 in our study is similar: the first H_2 production event occurs as the metal cations are reduced and a second more intense one when the particles are formed. A few H_2 are detected for Co alone but to a lower extent. This H_2 could be involved in the reduction of Co during the stage at the boiling temperature. For the compositions containing Ru, the H_2 is released in higher quantity, explaining the reduction of Co(II) concomitantly to Ru(III). When the particles are formed, they then catalyze the dehydrogenation of the alcohol solvent and then generate more H_2. A synergetic catalytic effect is then observed for mixed compositions. The nanoplatelet morphology of the nanoalloys can be explained by the fact that the close packed surface (0001) of the hcp structure is the most stable one.

5. Conclusions

Coupling various techniques such as UV-visible and X-ray absorption spectroscopies as well as chromatography or X-ray scattering techniques permits to follow the reduction of species and the modification of the environments of metal centers as well as the fate of the by-products in the liquid and gas phases. A good insight into the mechanism of formation of metal nanoparticles in solution can then be achieved. Depending on the metal ions, the reduction can be straightforward (for Ru(III) for example) or can involve the formation of intermediate species (formation of CoO for solutions containing only Co(II) metal cations, for example). The addition of a more reducible noble metal salt to a solution containing a transition metal salt can trigger its reduction, resulting in a quasi-simultaneous reduction of the two metal cations which leads to the formation of an alloy. In our system, our results suggest that the reducing agent is not only the solvent but also *in situ* generated H_2. More generally, this work opens perspectives for the formation of other nanoalloys of interest, using *in situ* generated H_2.

Author contributions

B. A., T. B. G. and N. H. achieved the synthesis of the nanoalloys under the supervision of L. S. and J.-Y. P. B. A. achieved the first synthesis in ITODYS and carried out the UV-visible spectroscopy measurements under the supervision of J. B. T. B. G. and N. H. carried out the chromatography experiments. O. T. made the SAXS measurements. L. B. designed the cell for *in situ* XAS experiments. B. A., S. N., J.-Y. P., V. B. and L. S. carried out the XAS experiments in SOLEIL, L. S. carried out the EXAFS treatment while V. B. carried out the PCA and MCR-ALS analysis. M. G., J. P., J.-Y. P. and L. S. debated about the experiments and their interpretation.

Conflicts of interest

There are no conflicts to declare.

Acknowledgements

This work was done as a part of the ANR TANOPOL project (ANR-15-CE07-0011-01). It benefited from a 2018 JSPS grant for B. Azeredo. Ning Huang thanks CSC for his PhD grant. SasView application, originally developed under NSF award DMR-0520547 was used. SasView contains code developed with funding from the European Union's Horizon 2020 research and innovation program under the SINE2020 project, grant agreement no. 654000. XAS measurements were supported by a public grant overseen by the French National Research Agency (ANR) as part of the ''Investissements d'Avenir'' program (reference: ANR-10-EQPX-45). The analysis of XAS results benefited from the use of Demeter software and MCR-ALS 2.0 Matlab® toolbox available freely. We acknowledge SOLEIL for provision of the synchrotron radiation facilities (ROCK beamline, Proposal number 20181004).

References

1 C. B. Murray, C. R. Kagan and M. G. Bawendi, Synthesis and Characterization of Monodisperse Nanocrystals and Close-Packed Nanocrystal Assemblies, *Annu. Rev. Mater. Sci.*, 2000, **30**, 545–610.

2 K. McNamara and S. A. M. Tofail, Nanosystems: the use of nanoalloys, metallic, bimetallic, and magnetic nanoparticles in biomedical applications, *Phys. Chem. Chem. Phys.*, 2015, **17**, 27981–27995.

3 Y. Xia, P. Yang, Y. Sun, Y. Wu, B. Mayers, B. Gates, Y. Yin, F. Kim and H. Yan, One-Dimensional Nanostructures: Synthesis, Characterization, and Applications, *Adv. Mater.*, 2003, **15**, 353–389.

4 Y. Xia, Y. Xiong, B. Lim and S. E. Skrabalak, Shape-controlled synthesis of metal nanocrystals: simple chemistry meets complex physics?, *Angew. Chem., Int. Ed.*, 2009, **48**, 60–103.

5 S. A. M. Ealia and M. P. Saravanakumar, A review on the classification, characterisation, synthesis of nanoparticles and their application, *IOP Conf. Ser. Mater. Sci. Eng.*, 2017, **263**, 32019.

6 J. D. Rimer, A. Chawla and T. T. Le, Crystal Engineering for Catalysis, *Annu. Rev. Chem. Biomol. Eng.*, 2018, **9**, 283–309.

7 S. Duan and R. Wang, Bimetallic nanostructures with magnetic and noble metals and their physicochemical applications, *Prog. Nat. Sci. Mater. Int.*, 2013, **23**, 113–126.

8 A. Dehghan Banadaki and A. Kajbafvala, Recent Advances in Facile Synthesis of Bimetallic Nanostructures: An Overview, *J. Nanomater.*, 2014, **2014**, 985948.

9 C.-J. Jia and F. Schüth, Colloidal metal nanoparticles as a component of designed catalyst, *Phys. Chem. Chem. Phys.*, 2011, **13**, 2457–2487.

10 D. Wang and Y. Li, Bimetallic nanocrystals: Liquid-phase synthesis and catalytic applications, *Adv. Mater.*, 2011, **23**, 1044–1060.

11 K. D. Gilroy, A. Ruditskiy, H. Peng, D. Qin and Y. Xia, Bimetallic Nanocrystals: Syntheses, Properties, and Applications, *Chem. Rev.*, 2016, **116**, 10414–10472.

12 M. M.-J. Li and S. C. E. Tsang, Bimetallic catalysts for green methanol production via CO2 and renewable hydrogen: a mini-review and prospects, *Catal. Sci. Technol.*, 2018, **8**, 3450–3464.

13 A. K. Singh and Q. Xu, Synergistic Catalysis over Bimetallic Alloy Nanoparticles, *ChemCatChem*, 2013, **5**, 652–676.

14 A. M. Robinson, J. E. Hensley and J. W. Medlin, Bifunctional Catalysts for Upgrading of Biomass-Derived Oxygenates: A Review, *ACS Catal.*, 2016, **6**, 5026–5043.

15 R. Ferrando, J. Jellinek and R. L. Johnston, Nanoalloys: From Theory to Applications of Alloy Clusters and Nanoparticles, *Chem. Rev.*, 2008, **108**, 845–910.

16 F. Fiévet, S. Ammar-Merah, R. Brayner, F. Chau, M. Giraud, F. Mammeri, J. Peron, J.-Y. Piquemal, L. Sicard and G. Viau, The polyol process: a unique method for easy access to metal nanoparticles with tailored sizes, shapes and compositions, *Chem. Soc. Rev.*, 2018, **47**, 5187–5233.

17 M. Ishijima, J. L. Cuya Huaman, S. Yokoyama, K. Shinoda, M. Uchikoshi, H. Miyamura and B. Jeyadevan, In situ spectroscopic studies of the one-pot synthesis of composition-controlled Cu–Ni nanowires with enhanced catalytic activity, *New J. Chem.*, 2018, **42**, 13044–13053.

18 K. Taniguchi, K. Shinoda, J. L. Cuya Huaman, S. Yokoyama, M. Uchikoshi, T. Matsumoto, K. Suzuki, H. Miyamura and B. Jeyadevan, Designed synthesis of highly catalytic Ni–Pt nanoparticles for fuel cell applications, *SN Appl. Sci.*, 2018, **1**, 124.

19 K. Takahashi, S. Yokoyama, T. Matsumoto, J. L. Cuya Huaman, H. Kaneko, J.-Y. Piquemal, H. Miyamura and J. Balachandran, Towards a designed synthesis of metallic nanoparticles in polyols – elucidation of the redox scheme in a cobalt–ethylene glycol system, *New J. Chem.*, 2016, **40**, 8632–8642.

20 M. Ishijima, T. Matsumoto, J. L. Cuya Huaman, K. Shinoda, M. Uchikoshi, K. Matsuo, K. Suzuki, H. Miyamura and J. Balachandran, Theoretical and Experimental Evaluation of the Reduction Potential of Straight-Chain Alcohols for the Designed Synthesis of Bimetallic Nanostructures, *Inorg. Chem.*, 2021, **60**, 9432–9441.

21 M. Ishijima, J. L. Cuya Huaman, H. Wakizaka, K. Suzuki, H. Miyamura and J. Balachandran, Strategy to Design-Synthesize Bimetallic Nanostructures Using the Alcohol Reduction Method, *Inorg. Chem.*, 2021, **60**, 14436–14445.

22 M. Tsuji, S. Hikino, R. Tanabe, M. Matsunaga and Y. Sano, Syntheses of Ag/Cu alloy and Ag/Cu alloy core Cu shell nanoparticles using a polyol method, *CrystEngComm*, 2010, **12**, 3900–3908.

23 B. Huang, H. Kobayashi, T. Yamamoto, S. Matsumura, Y. Nishida, K. Sato, K. Nagaoka, S. Kawaguchi, Y. Kubota and H. Kitagawa, Solid-Solution Alloying of Immiscible Ru and Cu with Enhanced CO Oxidation Activity, *J. Am. Chem. Soc.*, 2017, **139**, 4643–4646.

24 M. R. Axet and K. Philippot, Catalysis with Colloidal Ruthenium Nanoparticles, *Chem. Rev.*, 2020, **120**, 1085–1145.

25 M. B. Gawande, A. Goswami, F.-X. Felpin, T. Asefa, X. Huang, R. Silva, X. Zou, R. Zboril and R. S. Varma, Cu

and Cu-Based Nanoparticles: Synthesis and Applications in Catalysis, *Chem. Rev.*, 2016, **116**, 3722–3811.
26 F. Diehl and A. Y. Khodakov, Promotion of cobalt Fischer-Tropsch catalysts with noble metals: a review, *Oil Gas Sci. Technol.*, 2009, **64**, 11–24.
27 T. Wang, J. Ibañez, K. Wang, L. Fang, M. Sabbe, C. Michel, S. Paul, M. Pera-Titus and P. Sautet, Rational design of selective metal catalysts for alcohol amination with ammonia, *Nat. Catal.*, 2019, **2**, 773–779.
28 Y. Bao, J. Dai, J. Zhao, Y. Wu, C. Li, L. Ji, X. Zhang and F. Yang, Modulation in Ruthenium–Cobalt Electronic Structure for Highly Efficient Overall Water Splitting, *ACS Appl. Energy Mater.*, 2020, **3**, 1869–1874.
29 W. Li, Y. Zhao, Y. Liu, M. Sun, G. I. N. Waterhouse, B. Huang, K. Zhang, T. Zhang and S. Lu, Exploiting Ru-Induced Lattice Strain in CoRu Nanoalloys for Robust Bifunctional Hydrogen Production, *Angew. Chem., Int. Ed.*, 2021, **60**, 3290–3298.
30 D. Zitoun, M. Respaud, M.-C. Fromen, P. Lecante, M.-J. Casanove, C. Amiens and B. Chaudret, Bimetallic CoRh and CoRu nanoparticles: size-induced enhanced magnetisation, *J. Magn. Magn. Mater.*, 2004, **272–276**, 1536–1538.
31 R. K. Ramamoorthy, A. Viola, B. Grindi, J. Peron, C. Gatel, M. Hytch, R. Arenal, L. Sicard, M. Giraud, J.-Y. Piquemal and G. Viau, One-Pot Seed-Mediated Growth of Co Nanoparticles by the Polyol Process: Unraveling the Heterogeneous Nucleation, *Nano Lett.*, 2019, **19**, 9160–9169.
32 A. Viola, M. Peboscq, J. Peron, M. Giraud, L. Sicard, R. K. Ramamoorthy, B. Azeredo, S. Nowak, P. Decorse, G. Viau and J.-Y. Piquemal, Impact of noble-metals on the catalytic stability of cobalt nanoparticles for the acceptorless dehydrogenation of alcohols, *Catal. Today*, 2019, **333**, 97–104.
33 B. Azeredo, T. Ben Ghzaiel, N. Huang, K. Kaźmierczak, W. Shen, G. Wang, D. Schaming, P. Beaunier, P. Decorse, N. Perret, J. Peron, M. Giraud, C. Michel, L. Sicard and J.-Y. Piquemal, Co–Ru Nanoalloy Catalysts for the Acceptorless Dehydrogenation of Alcohols, *ACS Appl. Nano Mater.*, 2022, **5**, 5733–5744.
34 R. F. Zhang, X. F. Kong, H. T. Wang, S. H. Zhang, D. Legut, S. H. Sheng, S. Srinivasan, K. Rajan and T. C. Germann, An informatics guided classification of miscible and immiscible binary alloy systems, *Sci. Rep.*, 2017, **7**, 9577.
35 *CRC Handbook of Chemistry and Physics*, ed. D. R. Lide, CRC Press, Boca Raton, FL, 2005.
36 D. Saha, E. D. Bøjesen, A. H. Mamakhel, M. Bremholm and B. B. Iversen, In Situ PDF Study of the Nucleation and Growth of Intermetallic PtPb Nanocrystals, *ChemNanoMat*, 2017, **3**, 472–478.
37 C. La Fontaine, S. Belin, L. Barthe, O. Roudenko and V. Briois, ROCK: A Beamline Tailored for Catalysis and Energy-Related Materials from ms Time Resolution to μm Spatial Resolution, *Synchrotron Radiat. News*, 2020, **33**, 20–25.
38 A. R. Passos, C. La Fontaine, L. Martins, S. H. Pulcinelli, C. V. Santilli and V. Briois, Operando XAS/Raman/MS monitoring of ethanol steam reforming reaction–regeneration cycles, *Catal. Sci. Technol.*, 2018, **8**, 6297–6301.
39 C. Lesage, E. Devers, C. Legens, G. Fernandes, O. Roudenko and V. Briois, High pressure cell for edge jumping X-ray absorption spectroscopy: Applications to industrial liquid sulfidation of hydrotreatment catalysts, *Catal. Today*, 2019, **336**, 63–73.
40 A. de Juan, J. Jaumot and R. Tauler, Multivariate Curve Resolution (MCR). Solving the mixture analysis problem, *Anal. Methods*, 2014, **6**, 4964–4976.
41 J. Jaumot, A. de Juan and R. Tauler, MCR-ALS GUI 2.0: New features and applications, *Chemom. Intell. Lab. Syst.*, 2015, **140**, 1–12.
42 H. W. P. Carvalho, S. H. Pulcinelli, C. V. Santilli, F. Leroux, F. Meneau and V. Briois, XAS/WAXS Time-Resolved Phase Speciation of Chlorine LDH Thermal Transformation: Emerging Roles of Isovalent Metal Substitution, *Chem. Mater.*, 2013, **25**, 2855–2867.
43 W. H. Cassinelli, L. Martins, A. R. Passos, S. H. Pulcinelli, C. V. Santilli, A. Rochet and V. Briois, Multivariate curve resolution analysis applied to time-resolved synchrotron X-ray Absorption Spectroscopy monitoring of the activation of copper alumina catalyst, *Catal. Today*, 2014, **229**, 114–122.
44 A. Voronov, A. Urakawa, W. van Beek, N. E. Tsakoumis, H. Emerich and M. Rønning, Multivariate curve resolution applied to in situ X-ray absorption spectroscopy data: an efficient tool for data processing and analysis, *Anal. Chim. Acta*, 2014, **840**, 20–27.
45 J. Hong, E. Marceau, A. Y. Khodakov, L. Gaberová, A. Griboval-Constant, J.-S. Girardon, C. La Fontaine and V. Briois, Speciation of Ruthenium as a Reduction Promoter of Silica-Supported Co Catalysts: A Time-Resolved in Situ XAS Investigation, *ACS Catal.*, 2015, **5**, 1273–1282.
46 B. Ravel and M. Newville, ATHENA, ARTEMIS, HEPHAESTUS: data analysis for X-ray absorption spectroscopy using IFEFFIT, *J. Synchrotron Radiat.*, 2005, **12**, 537–541.
47 O. Taché, S. Rouzière, P. Joly, M. Amara, B. Fleury, A. Thill, P. Launois, O. Spalla and B. Abécassis, MOMAC: a SAXS/WAXS laboratory instrument dedicated to nanomaterials, *J. Appl. Crystallogr.*, 2016, **49**, 1624–1631.
48 Sasview, **https://www.sasview.org/**.
49 A. B. P. Lever, *Inorganic Electronic Spectroscopy*, Elsevier, Amsterdam, Netherlands, 2nd edn, 1984.
50 S. Duman, M. Masjedi and S. Özkar, Highly active and long lived homogeneous catalyst for the dehydrogenation of dimethylamine borane starting with ruthenium(III) acetylacetonate and oleylamine precatalyst, *J. Mol. Catal. A: Chem.*, 2016, **411**, 9–18.
51 C. Dong, X. Zhang, J. Xu, R. Si, J. Sheng, J. Luo, S. Zhang, W. Dong, G. Li, W. Wang and F. Huang, Ruthenium-Doped Cobalt–Chromium Layered Double Hydroxides for Enhancing Oxygen Evolution through Regulating Charge Transfer, *Small*, 2020, **16**, 1–7.
52 N. Chakroune, G. Viau, S. Ammar, L. Poul, D. Veautier, M. M. Chehimi, C. Mangeney, F. Villain and F. Fiévet, Acetate- and Thiol-Capped Monodisperse Ruthenium Nanoparticles: XPS, XAS, and HRTEM Studies, *Langmuir*, 2005, **21**, 6788–6796.

53 E. Iglesia, S. L. Soled, R. A. Fiato and G. H. Via, Bimetallic Synergy in Cobalt Ruthenium Fischer-Tropsch Synthesis Catalysts, *J. Catal.*, 1993, **143**, 345–368.
54 R. H. Crabtree, Homogeneous Transition Metal Catalysis of Acceptorless Dehydrogenative Alcohol Oxidation: Applications in Hydrogen Storage and to Heterocycle Synthesis, *Chem. Rev.*, 2017, **117**, 9228–9246.
55 M. Nielsen, A. Kammer, D. Cozzula, H. Junge, S. Gladiali and M. Beller, Efficient Hydrogen Production from Alcohols under Mild Reaction Conditions, *Angew. Chem., Int. Ed.*, 2011, **50**, 9593–9597.

